Research Square

Preprints are preliminary reports that have not undergone peer review.
They should not be considered conclusive, used to inform clinical practice,
or referenced by the media as validated information.

Vacancy order beyond complete local coordination in perovskites

Jiasheng Yang

2210623312@shu.edu.cn

Sino-European School of Technology, Shanghai University

Article

Keywords:

Posted Date: November 11th, 2026

DOI: https://doi.org/10.21203/rs.3.rs-11417376/v1

License: This work is licensed under a Creative Commons Attribution 4.0 International License.
Read Full License

Additional Declarations: No competing interests reported.

Vacancy order beyond complete local coordination in perovskites

Jiasheng Yang*
Sino-European School of Technology, Shanghai University, Shanghai 200444, China
*Correspondence: 2210623312@shu.edu.cn
ORCID: 0009-0005-7797-9290

Abstract

In oxygen-deficient perovskites, even the complete site-resolved coordination fields of both cation sublattices need not determine the oxygen-vacancy arrangement. Here we solve this information gap exactly on the perovskite parent network. A joint map from oxygen occupation to A- and B-site coordination gives the full compatibility conditions and separates finite-support coordination-preserving variations from additional periodic freedoms. At $ABO_{2.5}$ composition, differences between explicit binary orders span this nonlocal sector, and occupancy capacity makes a large exactly characterized subset rigid against every finite-support rearrangement preserving both coordination fields. A $CaMnO_{2.5}$ vacancy-order microdomain identified by electron diffraction and HREM maps exactly onto the minimal member of this rigid sector. A general domain-stitching identity then shows how changes between same-coordination orders reappear as interface defects. In a fully specified exchange channel, the optimal peak joint defect measure grows as 2L+2 although separately optimized A- and B-site peaks remain constant. Experimental bulk structures, vacancy-order domains and homologous intergrowths place the exact results within the broader coordination fibre.

Introduction

Ordered oxygen vacancies reorganize perovskites over length scales far beyond a single coordination polyhedron. Diffraction and electron microscopy have resolved vacancy superstructures, tetrahedral-chain order, stacking variants, antiphase boundaries, long-period order and order–disorder transitions in brownmillerites and related oxygen-deficient perovskites [1,2,3,4,5,6,7,8,9]. These arrangements can also change transport, magnetic and structural responses [7,10,11]. Coordination environments are therefore natural descriptors of oxygen-deficient structures. A more basic question remains: if the coordination of every A site and every B site is specified, has the oxygen-vacancy configuration itself been determined?

Existing approaches answer adjacent questions. Symmetry analysis enumerates crystallographically distinct anion orders [12]. Structure generation and first-principles calculations explore candidate vacancy patterns and the chemical or elastic factors that select among them [10,11,13,14]. Cation coordination preferences also organize [111] stacking designs across layered perovskite compositions [13,15]. Microscopy and diffraction identify the orders and defects realized in particular compounds [1,2,3,4,5,6,7]. These approaches do not determine what structural information is contained in the complete local coordination fields themselves. Because one oxygen site is shared by two B sites and four A sites in the perovskite parent network, the two coordination fields cannot be assigned independently. Conversely, even their complete site-resolved values need not uniquely specify the oxygen pattern. We ask which A/B fields can arise from one oxygen occupation, what structural freedom remains after both are fixed, and what is required to change that remaining order locally.

Translation-resolved constraint operators provide a useful language for this problem. In periodic framework and flat-band theories, singular symbols can separate compactly generated modes from additional periodic freedoms [16,17,18]. Related constrained lattice models show how local rules generate subextensive configuration families and suppress local rearrangements [19,20]. These results establish precedents for constraint-induced nonlocal

structure. Here, a single oxygen occupation field must reproduce both complete site-resolved cation coordination fields. We therefore seek the image, finite-support kernel, periodic residual freedom and binary realizability of this specific joint map.

Atomic occupation adds a second layer: an oxygen site is occupied or vacant. A signed linear kernel therefore need not describe a permitted rearrangement of a binary configuration, just as a linear or algebraic kernel basis need not connect a non-negative integer fibre [21]. The compatibility problem must retain both the complete linear kernel and the occupancy constraint.

Here we solve the joint oxygen-occupation–coordination map on the perovskite parent network. We first obtain the complete compatibility spectrum and the full finite-support coordination-preserving kernel. Their difference identifies a periodic sector that is invisible to all local A/B coordination counts. We then construct binary $ABO_{2.5}$ orders whose differences span this sector and show that occupancy capacity makes an explicit, exponentially growing subset locally rigid under coordination-preserving changes. An experimentally identified $CaMnO_{2.5}$ microdomain provides a direct structural instance of this extremal sector: its observed $(\sqrt{2}\times\sqrt{2})R45°$ parent supercell and all-square-pyramidal Mn coordination uniquely fix, up to translation and parent-axis exchange, the minimal checkerboard vacancy topology used in the theorem [1,22,23]. The same joint map gives a general relation between changes of same-coordination order and the coordination defects created at their boundaries, together with an exact quantitative separation in a solvable exchange problem. Experimental $Ca_2Mn_2O_5$ and $Sr_2Mn_2O_5$ structures and Sr–Mn homologous vacancy planes then show how the compatibility language organizes realized bulk order, registry changes and coherent intergrowth.

Results

Shared oxygen sites impose joint coordination constraints

We place B sites at integer parent coordinates n, A sites at n+(1/2,1/2,1/2), and the three oxygen sites at $n+e_j/2$, where j labels the parent axes. The binary variable $x_j(n)$ is one for a vacancy and zero for an occupied oxygen site. We count missing oxygens in the parent neighbour shells:

$$f_B(n)=\sum_j [\, x_j(n)+x_j(n-e_j)], \qquad f_A(n)=\sum_j \sum_{p,q=0}^{1} x_j\,(n+pe_k+qe_l), \tag{1}$$

where $\{j,k,l\}=\{x,y,z\}$. The coordination counts are $6-f_B$ and $12-f_A$. Equation (1) defines the joint map $f=Cx$ (Fig. 1a). A coordination fibre is the set of occupations giving the same complete site-resolved field f.

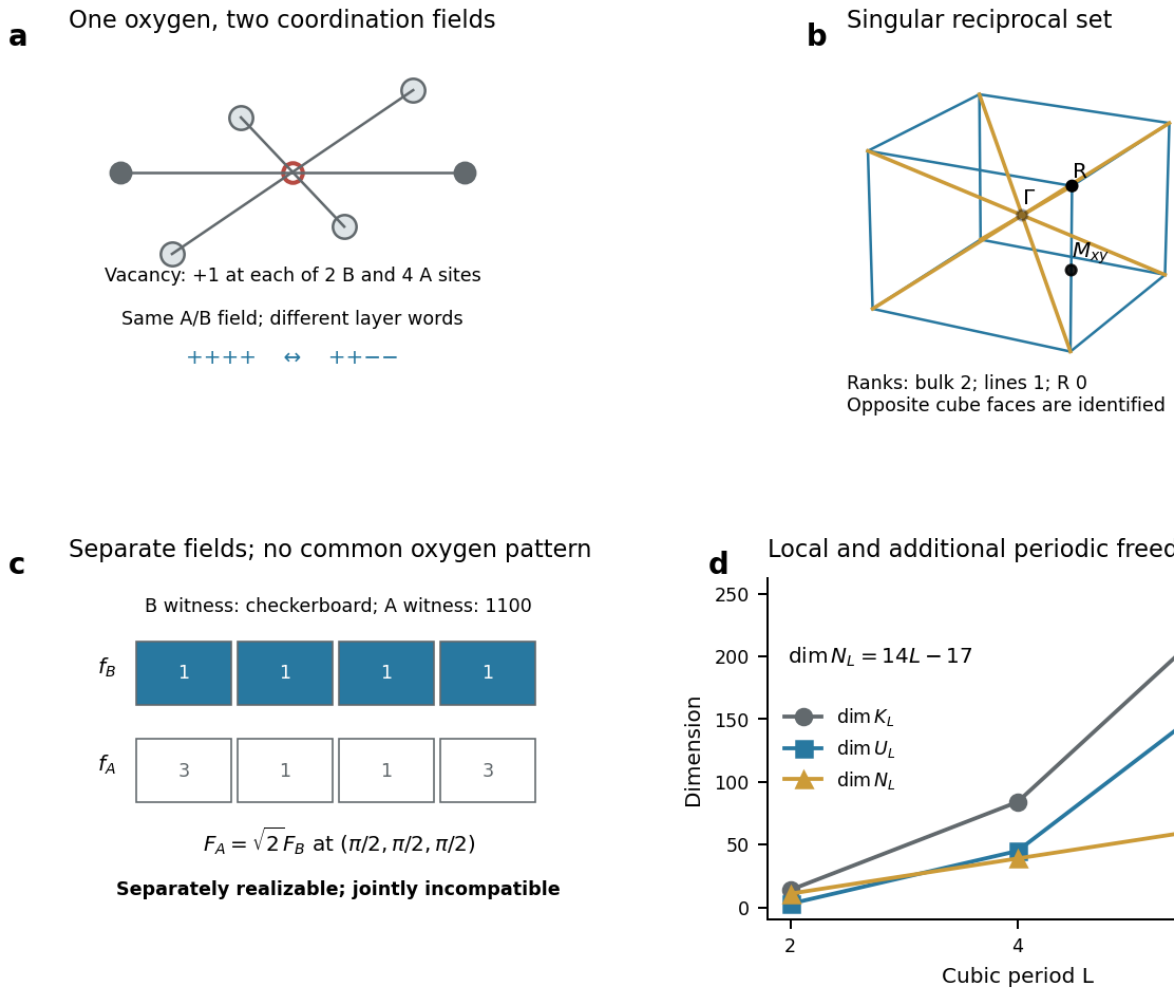


Figure 1 | Joint coordination compatibility on shared oxygen sites. a, Parent connectivity: one oxygen site is shared by two B sites and four A sites; f_B and f_A count missing neighbours. **b**, Complete rank-deficient set of the joint symbol, with four body-diagonal lines, three zone-edge lines and the rank-zero point R. Generic points have rank two. **c**, An L=4 target with uniform f_B=1 and f_A=(3,1,1,3) along diagonal layers. The two fields have separate binary realizations but violate the joint diagonal selection rule. **d**, Dimensions of the periodic kernel, periodized finite-support span and their difference for the displayed even periods. The nonlocal dimension is $14L-17$. All coordinates are parent coordinates.

Including the oxygen basis positions in the Fourier transform gives the symbol

$$C(k)=\begin{pmatrix} 2c_x & 2c_y & 2c_z \\ 4c_yc_z & 4c_xc_z & 4c_xc_y \end{pmatrix}, \qquad c_j=\cos(k_j/2). \tag{2}$$

The generic rank is two. It drops to one on four signed body diagonals and three zone-edge lines, and to zero at $R=(\pi,\pi,\pi)$. These are all rank-deficient points on the real reciprocal torus. We denote their union by Σ. At a diagonal point $k=(\pm t,\pm t,\pm t)$, compatibility requires $F_A=2\cos(t/2)F_B$; on a zone edge it requires $F_A=0$; at R both components vanish (Fig. 1b). For real periodic occupations, these pointwise conditions are necessary and sufficient. Binary occupation imposes the additional site-capacity condition.

A simple example shows why two separate coordination checks are insufficient. On a four-period parent lattice, take f_B=1 everywhere and let f_A cycle as (3,1,1,3) along $s=n_x+n_y+n_z$. Each target separately has a binary realization with the same vacancy number. Together they violate the diagonal selection rule at $k=(\pi/2,\pi/2,\pi/2)$: F_B vanishes there while F_A does not (Fig. 1c). Thus the desired A and B environments cannot coexist on one oxygen pattern.

The kernel also separates into local and nonlocal parts. Let K_L=kerC_L for an $L\times L\times L$ parent torus. Let U_L be the span of periodic images of all finite-support kernel vectors on the infinite parent lattice. A primitive Laurent vector G generates every such finite-support signed variation. Its Fourier value spans the generic one-dimensional kernel and vanishes exactly on Σ. Consequently,

$$K_L=U_L\oplus N_L, \qquad N_L=\oplus_{k\in\Sigma_L}\ker C(k), \tag{3}$$

with conjugate Fourier components paired for real fields. For even L,

$$\dim N_L=14L-17. \tag{4}$$

The corresponding odd-period dimension is $8L-6$. The distinction is between finite-support variations on the infinite network and additional periodic freedoms, not between short and long wavelengths. The Supplementary Notes “Parent adjacency, Fourier conventions and real compatibility”, “Complete finite-support kernel” and “Periodic decomposition and dimensions” give the complete kernel and counting proofs.

Binary occupation turns hidden modes into rigid vacancy structures

We now fix f_B=1 and f_A=2 at every site, corresponding to BO_5/AO_{10} and $ABO_{2.5}$. For even L, one family is

$$x_x(n)=\frac{1+(-1)^{n_x+n_y}H(n_z)}{2}, \qquad x_y=x_z=0, \tag{5}$$

where each H is independently +1 or -1. All 2^L layer sequences have identical A/B coordination. Their non-constant Fourier content lies on the zone edge (π,π,k_z). A second family uses $s=n_x+n_y+n_z$: empty layers alternate with vacancy-containing layers, and each vacancy-containing layer independently chooses one of the three oxygen orientations (Fig. 2a,b). The corresponding modes lie on a body diagonal.

These constructions are complete in two natural subspaces. If only one oxygen orientation can be vacant, every BO_5/AO_{10} structure belongs to one of two transverse checkerboard layer families obtained from equation (5) by interchanging axes. If the occupations depend only on s, every solution has the alternating empty/active-layer form. In both cases, integrality supplies the decisive restriction: a linear superposition allowed by equation (1) need not remain binary. The constructions also extend to non-periodic layer sequences on the infinite network.

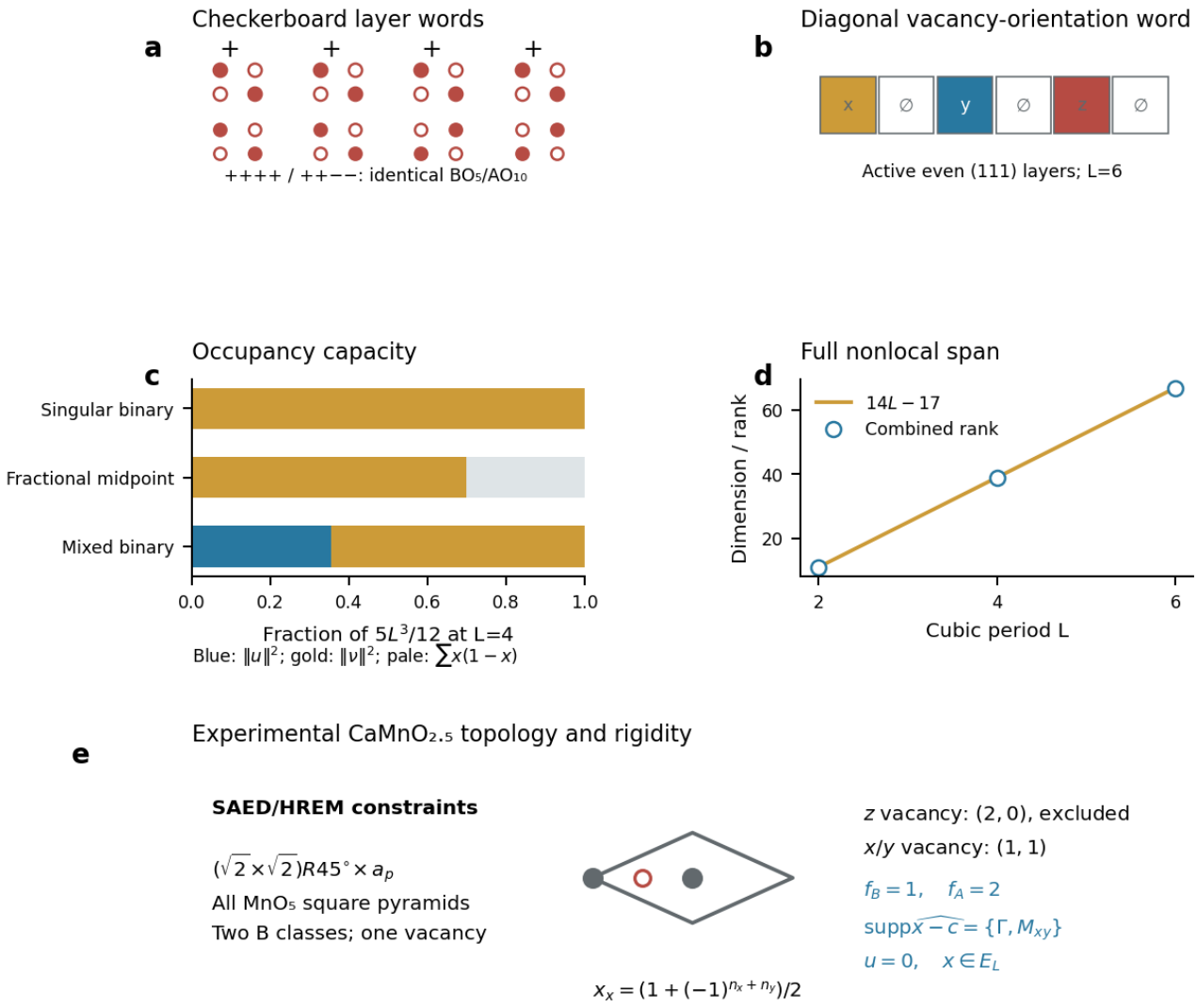


Figure 2 | Binary vacancy order and capacity rigidity. a, Two layer words in the zone-edge family, equation (5), with identical BO_5/AO_{10} coordination. **b**, A body-diagonal construction with alternating empty and vacancy-containing layers and an independent orientation choice on each active layer. **c**, Contributions to the occupancy identity for a purely singular binary state, a fractional midpoint of two layer words, and a mixed binary example. Each bar is normalized by $5L^3/12$ at L=4. Purely singular binary configurations exhaust this value through the nonlocal norm and admit no non-zero capacity-allowed change in the local span. **d**, Binary construction differences span the full nonlocal space at the displayed even sizes; the lines show the proved dimensions. **e**, **Experimental minimal rigid topology.** SAED/HREM studies of $CaMnO_{2.5}$ identified a $\sqrt{2}\times\sqrt{2}R45°$ vacancy-order microdomain in the all-MnO_5 endpoint [22,23]. The two-parent-cell supercell contains one vacancy. Uniform BO_5 excludes a vacancy along the unchanged parent axis and uniquely fixes, up to translation and axis exchange, the checkerboard topology shown. Direct evaluation gives f_B=1, f_A=2, and Fourier support only at Γ and M_{xy}, so the observed topology is a member of E_L. The examples illustrate constructions, not a list of thermodynamically selected phases.

Occupancy capacity gives a stronger consequence than multiplicity. Write any real solution in this fibre as

$$x=c+u+v, \quad c=1/6\,\mathbf{1}, \quad u\in U_L, \quad v\in N_L.$$

For $0 \le x \le 1$,

$$\|u\|^2+\|v\|^2+\sum_i x_i\,(1-x_i)=\frac{5L^3}{12}. \tag{6}$$

The explicit binary families have $u=0$. Denote all binary states with this property by E_L. If $x^0 \in E_L$ and a signed local variation $\delta \in U_L$ keeps $x^0+\delta$ inside the occupancy cube, then $\langle x^0,\delta\rangle=0$ and $\sum_i \delta_i=0$. At a vacant site $\delta \le 0$; at an occupied site $\delta \ge 0$. The two equalities force every component of δ to vanish. Hence

$$(x^0+U_L)\cap[0,1]^{3L^3}=\{x^0\}. \tag{7}$$

The same finite-support argument applies to the infinite, possibly non-periodic constructions. The linear map retains finite-support zero modes generated by G; occupancy capacity removes every admissible local direction at these extremal states. Their rigidity follows from the shared-neighbour constraints and binary capacity, without specifying a hopping energy.

Although each such state has no non-trivial local move preserving both coordination fields, differences between these states span the entire nonlocal space:

$$\mathrm{span}_{\mathbb{R}}(E_L-E_L)=N_L. \tag{8}$$

Thus no part of the nonlocal linear sector relies solely on fractional occupation. Moreover, $2^L \le |E_L| \le 2^{14L-17}$, so $\log|E_L|$ grows in proportion to L. This remains true after quotienting by the parent translations and cubic point group. The multiplicity grows exponentially in linear size, while its logarithm per volume tends to zero. The Supplementary Notes "Binary constructions and complete restricted classifications", "Capacity rigidity, dual criterion and nonlocal saturation" and "Hidden-coordinate geometry, counting and structural distance" give the classifications, rigidity criterion and symmetry count.

Experimental realization of the minimal rigid state

An early electron-diffraction and HREM study of reduced $CaMnO_3$ identified four distinct $CaMnO_{2.5}$ vacancy-order superstructures. The smallest has an in-plane $(\sqrt{2}\times\sqrt{2})R45°$ mesh with $c \simeq a_p$, while the $CaMnO_{2.5}$ endpoint is formed only from MnO_5 square pyramids [1,22,23]. These observations determine the parent vacancy topology without requiring a full atomic refinement of the microdomain. The supercell contains two parent B sites and one oxygen vacancy. Its translations may be chosen as

$$(1,1,0), \qquad (1,-1,0), \qquad (0,0,1).$$

A vacancy on a z-oriented oxygen edge would connect the same B translation class at both ends and would therefore give missing-oxygen counts 2 and 0 on the two B classes, inconsistent with uniform five-coordinate Mn. The vacancy must therefore lie on an x- or y-oriented edge; these choices are related by parent symmetry. Up to translation and axis exchange, the unique binary topology is

$$x_x(n)=\frac{1+(-1)^{n_x+n_y}}{2}, \qquad x_y=x_z=0,$$

the $H=+1$ member of Eq. (5).

Direct substitution gives

$$f_B(n)=1, \qquad f_A(n)=2$$

at every parent site. Relative to $c=\mathbf{1}/6$, its Fourier support is only at Γ and $M_{xy}=(\pi,\pi,0)$. The Γ component is proportional to $(2,-1,-1)$, and the M_{xy} component to $(1,0,0)$; both lie in the corresponding kernels of $C(k)$. Hence $u=0$ and this experimentally identified vacancy topology belongs to E_L (Fig. 2e; Supplementary Note "Experimental minimal rigid topology in $CaMnO_{2.5}$"). The capacity-rigidity theorem therefore applies directly to the observed microdomain topology: no non-zero finite-support occupation change can preserve both complete coordination fields while remaining within the occupancy bounds.

Experimental Pbam structures expose a different registry freedom

The experimental Pbam refinements of $Ca_2Mn_2O_5$ [24] and $Sr_2Mn_2O_5$ [2] provide coordinate-level tests of the parent description. Both map to a four-parent-cell translation lattice with columns (1,1,0), (2,-2,0) and (0,0,1). After expanding the reported symmetry operations, the occupied oxygen sites assign one-to-one to ten of its twelve parent oxygen edges (Fig. 3a). The missing sites are a y-edge anchored at (0,0,0) and an x-edge anchored at (1,0,0), modulo these translations. Direct neighbour counting gives $f_B=1$ and $f_A=2$ on every site.

These experimental decorations are not purely singular. Per four-parent-cell unit,

$$\|u\|^2=1, \qquad \|v\|^2=\frac{2}{3}. \tag{9}$$

Their regular components occur at $\pm(\pi/2,-\pi/2,0)$, while Γ and $M_{xy}=(\pi,\pi,0)$ carry singular components. The observed order therefore occupies the broader coordination fibre, rather than only the rigid construction sector.

For $Ca_2Mn_2O_5$, the same mapping gives a reciprocal-space interpretation of the reported diffraction pattern. An orthorhombic reflection (h,k,l) maps to parent reciprocal-lattice units (h/2+k/4,h/2-k/4,l). The indexed (131) and (061) reflections [24] belong to regular and singular classes, respectively. The two ideal vacancy sites give non-zero vacancy contrast at both reflections (Fig. 3b). This connects the decomposition to identifiable reciprocal classes; the full measured intensities also contain the refined atomic displacements.

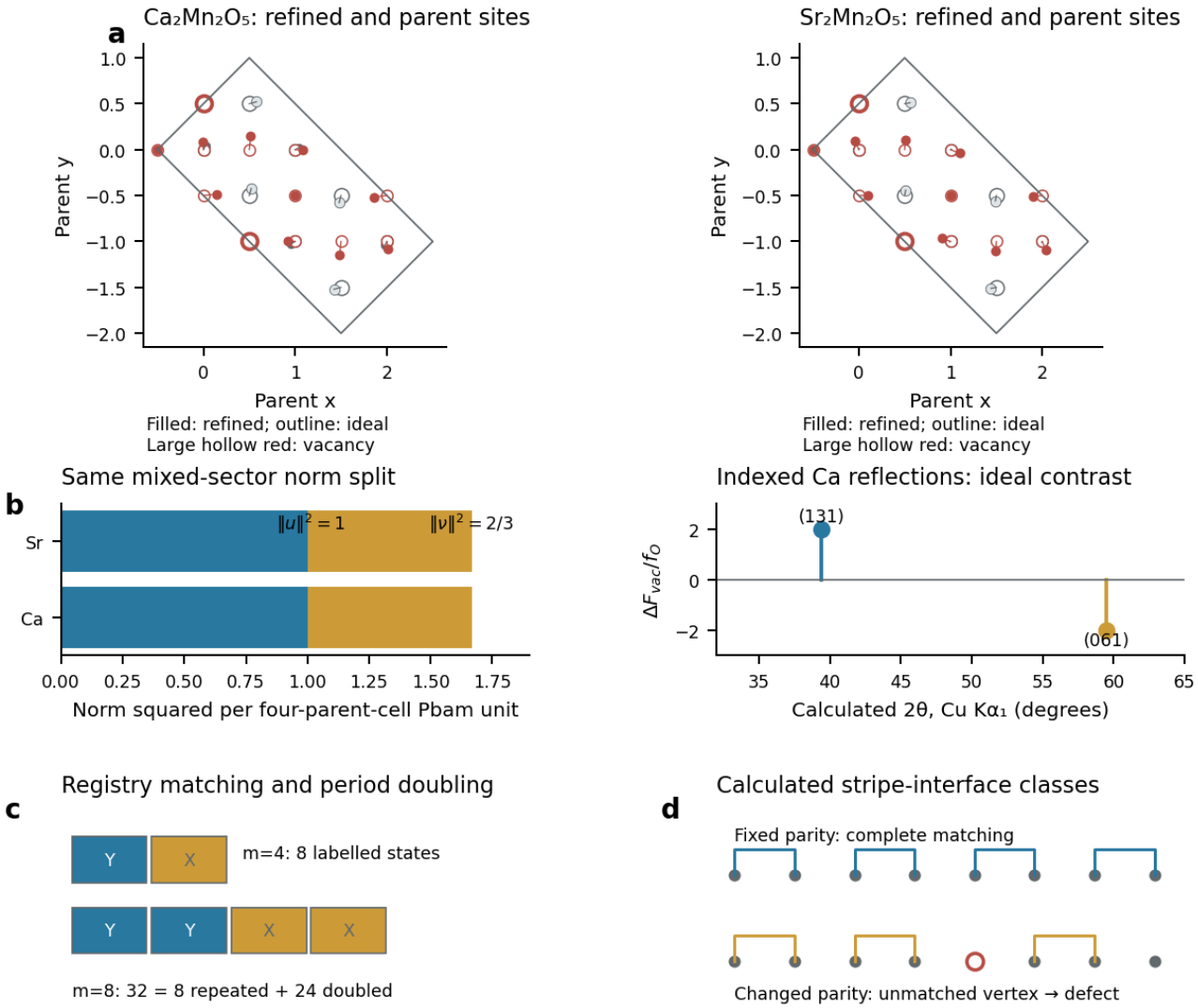


Figure 3 | Experimental Pbam order and registry constructions. a, Parent-site assignments of the refined $Ca_2Mn_2O_5$ [24] and $Sr_2Mn_2O_5$ [2] coordinates, with the same two missing oxygen edges. Parent idealization and refined positions are distinguished. **b**, Per four-parent-cell norm split, $\|u\|^2=1$ and $\|v\|^2=2/3$, and representative Ca reflections: (131) is in a regular reciprocal class, (061) in a singular class. The displayed contrasts are ideal vacancy amplitudes, not measured intensities. **c**, The Sr stripe coordinate $r=n_y-n_x$ reduces uniform BO_5/AO_{10} occupation to a two-labelled matching. A four-period cell has eight labelled solutions; an eight-period cell has 24 genuinely doubled solutions in addition to the eight repeated ones. **d**, Fixed-parity registry boundaries can preserve both coordination counts; a parity change requires a coordination defect within this stripe subspace. These are calculated boundary classes motivated by the microscopy of ref. 3, not assignments of individual micrographs.

The Pbam topology suggests the registry coordinate $r=n_y-n_x$. In the stripe subspace invariant along (1,1,0) and the third parent axis, let X_r and Y_r denote the two oxygen-edge vacancy occupations. Equation (1) becomes

$$f_B(r)=X_r+X_{r+1}+Y_r+Y_{r-1}, \qquad f_A(r)=2f_B(r). \tag{10}$$

Uniform BO_5/AO_{10} occupation is exactly a perfect matching of a one-dimensional cycle with two alternative edge labels on each matched pair. For even registry period $m\geq4$ there are two matching parities, and each of the m/2 pairs independently chooses X or Y. The complete labelled count is $2^{m/2+1}$.

The ordinary m=4 period has eight states. Doubling it to m=8 gives 32, of which 24 genuinely require the doubled registry period (Fig. 3c). This provides exact candidates with the enlarged periodicity reported in $Sr_2Mn_2O_5$ microscopy [3]. Within a fixed matching parity, changing the X/Y label sequence produces an aligned registry boundary without changing any A/B count. Changing the matching parity instead requires a degree defect in this stripe subspace. Translational variants shifted by two registry units preserve parity and differ only in regular modes; shifts by one unit also change the M_{xy} singular component.

The construction thus distinguishes two possible kinds of antiphase boundary in the same Pbam order. It supplies atomistic candidates consistent with the reported domain and stacking-fault classes [3], while the published bulk coordinates alone do not assign a particular microscopic boundary to one of these candidates. Supplementary Note "Pbam coordinate mappings and registry constructions" gives the complete registry construction and its spectral correspondence.

Local rewriting converts hidden order into coordination defects

The relation between bulk order and an interface follows directly from C. Let two binary endpoint structures have the same field, $Cx^0=Cx^1=f$, and set $\delta=x^1-x^0$. A spatial patchwork $y=x^0+\eta\delta$ chooses one endpoint at each oxygen site. For any corresponding cation mask η_c,

$$d_c=(Cy-f)_c=\sum_o C_{co}\,(\eta_o-\eta_c)\delta_o. \tag{11}$$

Only neighbours crossing a change in the mask can contribute. In particular, locally replacing a rigid background by a different same-fibre structure must leave coordination defects at the boundary of a finite patch (Fig. 4a). The identity applies to arbitrary three-dimensional endpoint decorations; it also permits cancellations for compatible aligned boundaries such as those above.

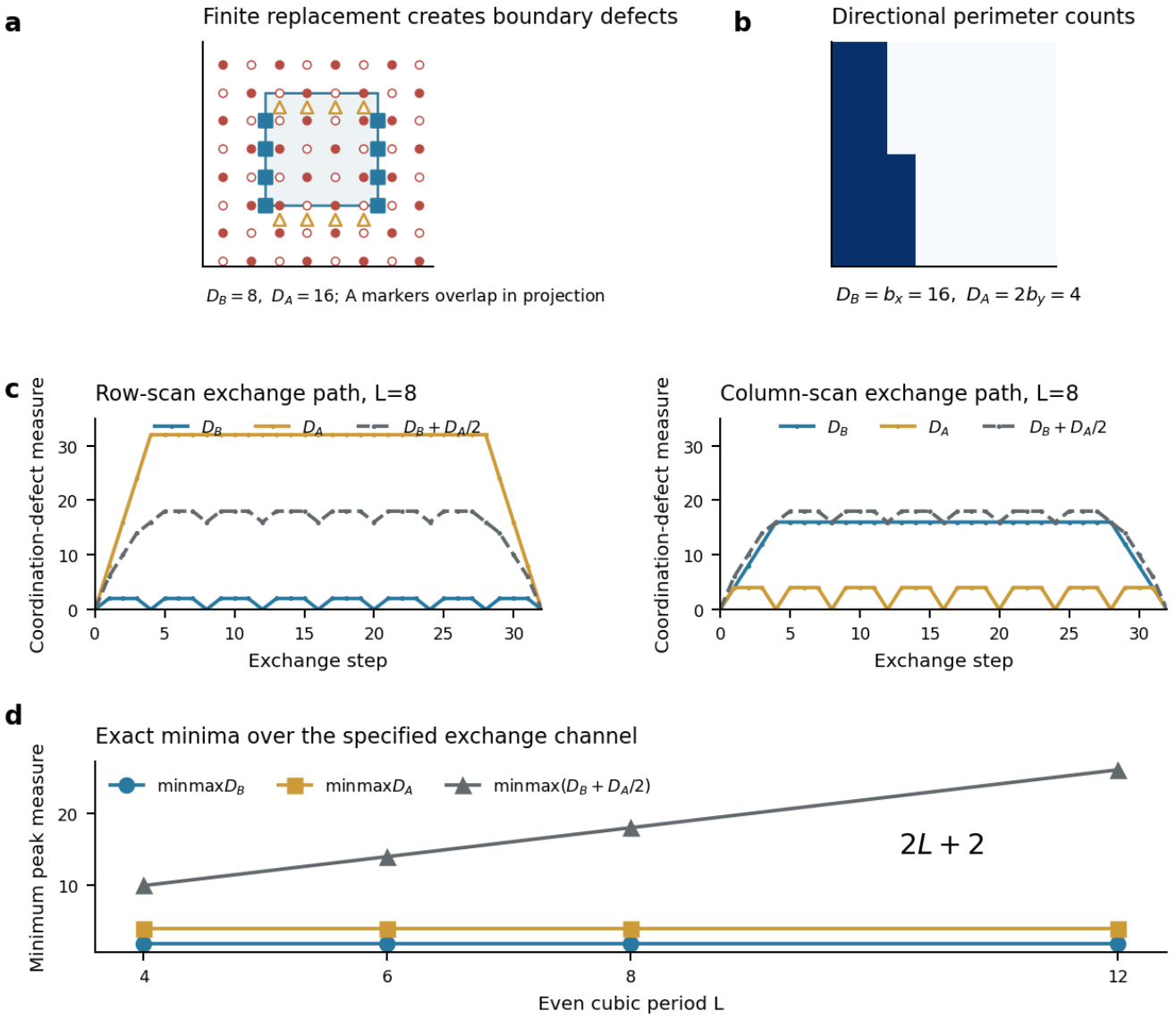


Figure 4 | Defects generated by local rewriting. a, A finite patch of one same-fibre structure within another. Equation (11) confines possible coordination defects to neighbour incidences crossing the patch boundary. **b**, In the single-layer, single-orientation periodic channel, a binary flip mask produces B and A defects on perpendicular parts of its boundary, with $D_B{=}b_x$ and $D_A{=}2b_y$. **c**, Row- and column-scan exchange paths at L=8 show how minimizing one coordination measure transfers defects to the other. Each path takes $L^2/2$ exchanges. **d**, Exact optimum values over the same path set: 2 for D_B, 4 for D_A, and 2L+2 for $D_B{+}D_A/2$, for even $L{\geq}4$. These are peak coordination-defect measures, not energy barriers.

The defect geometry carries information about the rearrangement. For a finite occupation change, write $T_j{=}\sum_n \delta\, x_j(n)$, $T{=}\sum_j T_j$. The difference between the A-defect second moment and twice the B-defect second moment is exactly

$$Q{=}\sum_A d_A\, r_A r_A^{\mathrm{T}} {-} 2\sum_B d_B\, r_B r_B^{\mathrm{T}} {=} TI {-} 2\mathrm{diag}(T_x,T_y,T_z). \tag{12}$$

Its zeroth and first moments vanish. Thus a number-conserving transfer between vacancy orientations requires a definite traceless coordination-defect second moment. At R, the corresponding staggered structural amplitudes are recovered from first moments of B defects. More generally, the singular amplitudes of any finite change follow

from first-order defect moments, with second order needed at Γ. These relations follow from the symmetry and derivatives of equation (2), as shown in Supplementary Note "Domain restriction and defect moments".

A fully solvable switching problem makes the effect of joint coordination quantitative. Take one layer of equation (5) on an even $L\times L$ periodic cross-section and reverse its layer sign. Only that layer and oxygen orientation may change, through nearest-neighbour oxygen/vacancy exchanges. Every binary intermediate state is specified by a mask η indicating the flipped sites. Direct substitution gives $D_B=\|d_B\|_1=b_x$ and $D_A=\|d_A\|_1=2b_y$, where b_x and b_y are the two directional boundary lengths of η. Therefore

$$\mathcal{D}=D_B+1/2\,D_A=|\partial\eta|.$$

This boundary-length formulation is closely related to communication-height results for periodic Ising and Potts models [25,26]. Here the optimization uses the specified vacancy-exchange graph and the physical A- and B-site defect variables. Over the same set of allowed paths γ,

$$\inf_{\gamma}\max_{t} D_B=2, \qquad \inf_{\gamma}\max_{t} D_A=4, \qquad \inf_{\gamma}\max_{t} \mathcal{D}=2L+2 \quad (L\geq 4). \tag{13}$$

The factor 1/2 removes duplication of the A-interface contribution on two neighbouring layers. It is a counting convention, not an energetic weight.

The lower bound follows because every path crosses half coverage. A half-covered torus has perimeter at least 2L; equality occurs only for a straight strip, and a legal exchange next to such a strip raises the perimeter by at least two. A row-by-row path attains 2L+2 in the minimum possible $L^2/2$ exchanges. It keeps $D_B\leq 2$ while D_A reaches 4L. A column-by-column path instead keeps $D_A\leq 4$ while D_B reaches 2L (Fig. 4b–d). Each individual objective can therefore transfer the coordination disturbance to the other sublattice. No path in this channel keeps the joint disturbance bounded independently of L. The complete proof and inverse reconstruction of a mask from its defects are in Supplementary Note "Complete single-layer channel and exact switching extremum".

A vacancy-plane rule permits coherent homologous intergrowth

The strontium manganites $Sr_{4+n}Mn_{4+n}O_{10+3n}$ provide a material-specific application beyond uniform coordination. Their established members include n=0,1,3, and their structures have been organized using MnO_5/MnO_6 building blocks [4,5]. A published HR-TEM report describes vacancy lines in (310) parent planes and coherent n=1/n=3 growth on opposite sides of a shared vacancy plane [27]. We use that reported plane geometry to construct the corresponding parent oxygen pattern.

Let $s=3n_x+n_y$ and let R be the integer set of vacancy-plane anchors. Put x-oriented vacancies at $s\in R$ and y-oriented vacancies at $s-1\in R$. Their oxygen-edge centres share the plane coordinate r+3/2. With I the indicator of R, equation (1) gives

$$\begin{aligned} f_B(s)&=I(s)+I(s-1)+I(s-2)+I(s-3),\\ f_A(s)&=2[I(s-1)+I(s)+I(s+1)+I(s+2)]=2f_B(s+2). \end{aligned} \tag{14}$$

Within this motif, having only BO_5/BO_6 and AO_{10}/AO_{12} is equivalent to requiring every consecutive plane spacing to be at least four. If two anchors are closer, a four-site window contains both and a lower B coordination appears. If all spacings are at least four, no window contains more than one anchor. This proves both necessity and sufficiency for the stated coordination palette, including non-periodic spacing sequences.

A uniform spacing m=n+4 gives two vacancies per m parent cells, hence O/B=3-2/m and exactly the homologous composition. It has four BO_5 and four AO_{10} sites, plus n BO_6 and n AO_{12} sites per repeat. At m=4 this motif reduces, up to a registry shift, to the mapped Pbam decoration. The coordination words along the two in-plane parent directions advance through the registry by one and three, respectively, reproducing the canonical building sequences [5].

Choosing spacings five on one side of a shared plane and seven on the other introduces no new coordination class at the junction. Alternating 5/7 spacings gives a 12-parent-cell repeat with eight BO_5, four BO_6, eight AO_{10} and four AO_{12} sites, and average O/B=8/3 (Fig. 5). This is a constructive coordination-compatible realization of the n=2 average composition through n=1/n=3 intergrowth, consistent with the reported microstructural possibility [27]. Uniform spacing six is also compatible. The rule therefore explains the structural admissibility of the intergrowth, while the selection between it and a homogeneous n=2 arrangement requires additional material information. Supplementary Note "Homologous vacancy planes and intergrowth" separates this palette comparison from equality of complete site-resolved fields.

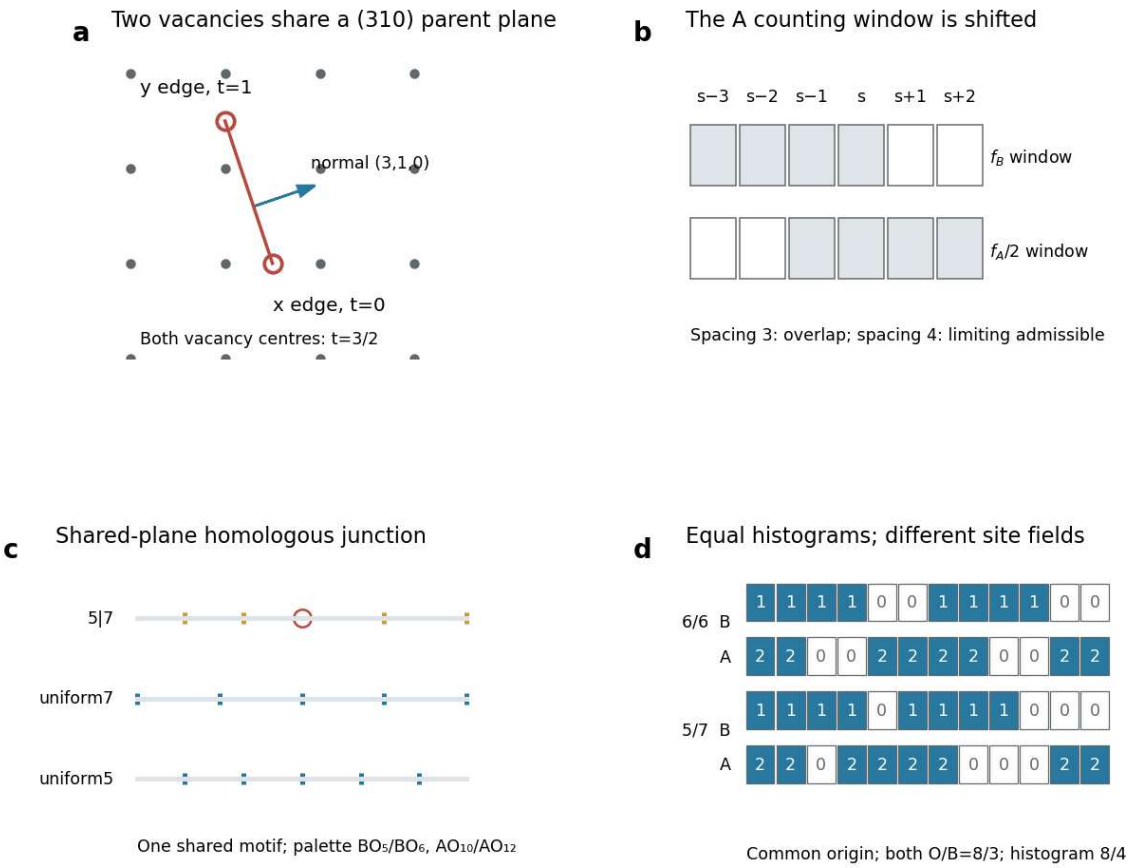


Figure 5 | Vacancy-plane spacing and homologous intergrowth. a, The two-edge motif on a (310) parent vacancy plane. **b**, Four-site windows of the anchor indicator give the B field and a shifted A field, equation (14). Spacings at least four are exactly those retaining the BO_5/BO_6 and AO_{10}/AO_{12} palette within this motif. **c**, Uniform spacings five and seven, and a shared-plane 5|7 junction, provide parent constructions corresponding to the reported homologous geometry [4,5,27]. **d**, Alternating 5/7 and uniform 6 spacings have the same average O/B=8/3 and coordination histograms but different site-resolved fields. Both are coordination-compatible. The diagram establishes admissibility of the intergrowth; it is not an energetic ranking of the two structures.

Discussion

Vacancy ordering, stacking variants and local order–disorder phenomena are well established in oxygen-deficient perovskites [3,5,6,7,8,9,10,11]. The present result concerns a different level of the structural problem: the information content of local coordination itself. Even when the coordination of every A and every B site is specified, the oxygen configuration need not be unique. At the same time, the two coordination fields cannot be prescribed independently because they are generated by the same shared oxygen sites. The joint map makes both statements exact: its image gives the compatibility conditions, while the difference between its finite-support and periodic kernels identifies structural information that complete local coordination does not contain.

Binary occupation changes the meaning of this remaining freedom. The growth $\log|E_L|=\Theta(L)$ places the rigid family among systems with subextensive configuration multiplicity [19,20,28]. In the present coordination problem, every state retains the same complete A/B fields, and differences of the rigid binary states span N_L. Each such state nevertheless admits no non-zero finite-support change preserving both fields and occupancy capacity. Thus coordination-invisible order is not simply a continuous null direction available to an atomic configuration. When a same-coordination structure is introduced only in a finite region, the joint map converts the structural difference into boundary coordination defects. Equation (11) gives this relation for arbitrary three-dimensional endpoint decorations, while equation (13) provides one fully solved quantitative example: within its specified exchange channel, separately minimizing either cation-sublattice defect measure keeps that optimum constant, whereas the joint optimum grows as 2L+2. The separation is a consequence of the shared oxygen constraint rather than of an assumed energetic penalty.

The material mappings span both an extremal and the broader parts of the compatibility fibre. Most directly, the smallest $CaMnO_{2.5}$ vacancy-order microdomain identified by SAED/HREM has the $(\sqrt{2}\times\sqrt{2})R45°$ parent mesh and all-square-pyramidal Mn coordination that uniquely force the minimal checkerboard E_L topology. The capacity-rigidity theorem therefore applies to this experimentally identified topology. The more common Pbam $Ca_2Mn_2O_5$ and $Sr_2Mn_2O_5$ structures instead occupy mixed regular/nonlocal sectors of the same BO_5/AO_{10} fibre, showing that realized structures need not sit at the extremal singular states. The $Sr_2Mn_2O_5$ registry reduction and the Sr–Mn homologous vacancy-plane construction then show how longer-period order, registry changes and coherent intergrowth can occur within or between such coordination descriptions. Together these cases separate an exact extremal limit from the wider structural fibre realized by the same class of oxygen-deficient perovskites.

Methods

Parent representation and proofs

All coordination counts refer to the inherited perovskite neighbour network in equation (1). We use vacancy indicators rather than occupied-oxygen indicators throughout. Real-linear compatibility is proved mode by mode. Completeness of the finite-support kernel uses a primitive Laurent generator, not just a numerical null vector. Periodic real dimensions pair conjugate characters. General supercells use their own translation-character set; the cubic formula $14L-17$ is not applied to a four-cell orthorhombic unit. The Supplementary Notes from “Parent adjacency, Fourier conventions and real compatibility” through “Complete single-layer channel and exact switching extremum” contain the derivations.

Experimental structure mapping

$Ca_2Mn_2O_5$ fractional coordinates and cell parameters were transcribed from Table S1 of the supporting information to ref. 24: a=5.4302 Å, b=10.2322 Å and c=3.7443 Å. $Sr_2Mn_2O_5$ uses the crystallographic record of ref. 2, COD 1001352, revision 130149. The Pbam symmetry orbits were expanded before assignment. In both structures, parent coordinates are $p=Sf-o$ with S columns (1,1,0), (2,-2,0), (0,0,1) and o=(1/2,0,0). B sites map to integer coordinates, A sites to half-translated integer coordinates, and occupied oxygen sites to parent edge centres. A one-to-one oxygen assignment was solved in the reported orthorhombic metric. The largest oxygen displacements from the assigned parent sites are 0.546 Å for Ca and 0.397 Å for Sr; the smallest nearest-versus-next-nearest assignment gaps are 1.722 Å and 2.057 Å. These are geometric assignment diagnostics, not uncertainties of the refinements. Complete numerical mappings are in Supplementary Tables S1 and S2 and the source data.

Reciprocal contrast and material-derived constructions

For the ideal parent vacancy contrast we evaluate the finite structure-factor sum over missing sites. The Ca (131)/(061) labels were checked against the indexed figure accompanying ref. 24. Coordinates and indexed reflections come from the same refinement, so the comparison supplies a consistent reciprocal interpretation rather than an independent intensity fit. The Sr homologous construction uses the reported vacancy-plane geometry [4,5,27] and nominal ordered vacancy sites; partially occupied sites in the refinements represent average occupations and are kept separate from the binary models. A 12-layer homometric example, following the standard distinction between a structure and its autocorrelation [29], documents why intensity alone need not reconstruct the phase-sensitive hidden coordinates.

Computation and reproducibility

Neighbour counts are evaluated directly on integer occupation arrays. Symbolic polynomial identities verify the Laurent generator and its primitivity. Small periodic instances cross-check rank formulas, binary classifications and symmetry counts. Exhaustive L=4 path checks use a finite state graph; constructive paths are also checked at larger L. The general results are proved independently of these finite checks. The supplied programs record input parameters and output checks, and the site-resolved relation in equation (14) is verified against the full three-dimensional neighbour operator. No new measurements or density-functional calculations were performed for this study.

Use of artificial intelligence

GPT-5 family models accessed through ChatGPT (OpenAI) assisted with code development, mathematical formalization, protocol-consistency and implementation checks, and computational documentation. All reported computational results were obtained by executing the finalized, author-reviewed code using the stated inputs and configurations. Generative AI was not used to generate, fabricate, or alter the reported numerical results or experimental data.

During the preparation of this work, the author used ChatGPT (OpenAI; GPT-5 family) for English-language refinement and clarity and consistency checks. The author reviewed and edited the adopted content as needed and takes full responsibility for the content of the article.

Data availability

The source data underlying the main and supplementary figures and tables, together with provenance records and derived data, are deposited in a private Zenodo record for peer review. Editors and reviewers can access the data through the following private preview link:

https://zenodo.org/records/23208593?preview=1&token=eyJhbGciOiJIUzUxMiJ9.eyJpZCI6IjI3YjI0ODUwLWE3ZjctNGQ0My04ZjA2LWVlZWJmY2NmN2EzOSIsImRhdGEiOnt9LCJyYW5kb20iOiI0ZDQ4MjlmZTI3MDBjODEwMzFkNDQzMzNlZjE3OTk4MCJ9.PkmH_12JfUExKJGyIv8AJI-S-24RWL4IP2W84CkVedmwMqnqChfTLzQMDfJCOa7yF6gok93-VTZUxADmxHjWdA

The record will be made publicly available with a persistent DOI before publication.

Code availability

The scientific verification code and associated inputs are included in the same Zenodo record and are available to editors and reviewers during peer review. The code archive will be made publicly available before publication.

References

1. Poeppelmeier, K. R., Leonowicz, M. E., Scanlon, J. C., Longo, J. M. & Yelon, W. B. Structure determination of $CaMnO_3$ and $CaMnO_{2.5}$ by X-ray and neutron methods. *Journal of Solid State Chemistry* **45**, 71–79 (1982). https://doi.org/10.1016/0022-4596(82)90292-4
2. Caignaert, V., Nguyen, N., Hervieu, M. & Raveau, B. $Sr_2Mn_2O_5$, an oxygen-defect perovskite with Mn(III) in square pyramidal coordination. *Materials Research Bulletin* **20**, 479–484 (1985). https://doi.org/10.1016/0025-5408(85)90101-1
3. Caignaert, V., Hervieu, M., Nguyen, N. & Raveau, B. The oxygen defect perovskite $Sr_2Mn_2O_5$: HREM study. *Journal of Solid State Chemistry* **62**, 281–289 (1986). https://doi.org/10.1016/0022-4596(86)90242-2
4. Suescun, L., Chmaissem, O., Mais, J., Dabrowski, B. & Jorgensen, J. D. Crystal structures, charge and oxygen-vacancy ordering in oxygen deficient perovskites SrMnOx (x<2.7). *Journal of Solid State Chemistry* **180**, 1698–1707 (2007). https://doi.org/10.1016/j.jssc.2007.03.020
5. Suescun, L. & Dabrowski, B. $Sr_{4+n}Mn_4^{3+}Mn_n^{4+}O_{10+3n}$: a new homologous series of oxygen-vacancy-ordered perovskites built from $Mn^{3+}O_5$ pyramids and $Mn^{4+}O_6$ octahedra. *Acta Crystallogr B Struct Sci* **64**, 177–186 (2008). https://doi.org/10.1107/s0108768108002760
6. D'Hondt, H. et al. Tetrahedral Chain Order in the $Sr_2Fe_2O_5$ Brownmillerite. *Chem. Mater.* **20**, 7188–7194 (2008). https://doi.org/10.1021/cm801723b
7. Auckett, J. E., Lee, W. T., Rule, K. C., Bosak, A. & Ling, C. D. Order, disorder, and dynamics in brownmillerite $Sr_2Fe_2O_5$. *Inorg. Chem.* **58**, 12317–12324 (2019). https://doi.org/10.1021/acs.inorgchem.9b01846
8. Abakumov, A. M., Rozova, M. G. & Antipov, E. V. Complex manganese oxides with the brownmillerite structure: synthesis, crystal chemistry and properties. *Russ. Chem. Rev.* **73**, 847–860 (2004). https://doi.org/10.1070/rc2004v073n09abeh000917

9. Subramani, T., Voskanyan, A., Jayanthi, K., Abramchuk, M. & Navrotsky, A. A Comparison of Order-Disorder in Several Families of Cubic Oxides. *Front. Chem.* **9**, 719169 (2021). https://doi.org/10.3389/fchem.2021.719169

10. Shin, Y. & Rondinelli, J. M. Magnetic structure of oxygen-deficient perovskite nickelates with ordered vacancies. *Phys. Rev. Research* **4**, L022069 (2022). https://doi.org/10.1103/physrevresearch.4.l022069

11. Han, Y., Shin, Y. & Galli, G. Engineering Intermediate Phases in Topotactic Phase Transitions of Cobaltite Perovskites. *Chemistry of Materials* **38**, 8357–8365 (2026). https://doi.org/10.1021/acs.chemmater.6c01174

12. Talanov, M. V., Shirokov, V. B. & Talanov, V. M. Anion order in perovskites: a group-theoretical analysis. *Acta Crystallogr A Found Adv* **72**, 222–235 (2016). https://doi.org/10.1107/s2053273315022147

13. Shin, Y., Poeppelmeier, K. R. & Rondinelli, J. M. Informatics-Based Learning of Oxygen Vacancy Ordering Principles in Oxygen-Deficient Perovskites. *Inorg. Chem.* **63**, 12785–12802 (2024). https://doi.org/10.1021/acs.inorgchem.4c01198

14. Molinari, M., Tompsett, D. A., Parker, S. C., Azough, F. & Freer, R. Structural, electronic and thermoelectric behaviour of $CaMnO_3$ and $CaMnO_{3-\delta}$. *J. Mater. Chem. A* **2**, 14109–14117 (2014). https://doi.org/10.1039/c4ta01514b

15. Nagase, T. et al. Cation Coordination Preferences toward Stacking Design in Layered Perovskites along the Perovskite [111] Direction. *J. Am. Chem. Soc.* **148**, 36630–36639 (2026). https://doi.org/10.1021/jacs.6c06507

16. Power, S. C. Polynomials for crystal frameworks and the rigid unit mode spectrum. arXiv:1102.2744, version 3 (2013). https://arxiv.org/abs/1102.2744

17. Bergman, D. L., Wu, C. & Balents, L. Band touching from real-space topology in frustrated hopping models. *Phys. Rev. B* **78**, 125104 (2008). https://doi.org/10.1103/physrevb.78.125104

18. Rhim, J. W. & Yang, B. J. Classification of flat bands according to the band-crossing singularity of Bloch wave functions. *Phys. Rev. B* **99**, 045107 (2019). https://doi.org/10.1103/physrevb.99.045107

19. Knowles, A. & Ganesh, R. Trivalent network model for d3 transition metal dichalcogenides in the 1T structure: Holography from local constraints. *Phys. Rev. B* **112**, 075101 (2025). https://doi.org/10.1103/knrx-g53z

20. Knowles, A. & Ganesh, R. Structures of group-15 elemental solids from an effective boundary theory. *Phys. Rev. B* **113**, 064104 (2026). https://doi.org/10.1103/v5sq-tn8z

21. Diaconis, P. & Sturmfels, B. Algebraic algorithms for sampling from conditional distributions. *Ann. Statist.* **26**, 363–397 (1998). https://doi.org/10.1214/aos/1030563990

22. Reller, A., Jefferson, D. A., Thomas, J. M., Beyerlein, R. A. & Poeppelmeier, K. R. Three new ordering schemes for oxygen vacancies in $CaMnO_{3-x}$: superlattices based on square-pyramidal co-ordination of Mn^{3+}. *J. Chem. Soc., Chem. Commun.* 1378–1380 (1982). https://doi.org/10.1039/c39820001378

23. Reller, A., Thomas, J. M., Jefferson, D. A. & Uppal, M. K. Superstructures formed by the ordering of vacancies in a selective oxidation catalyst: grossly defective $CaMnO_3$. *Proceedings of the Royal Society of*

London. A. Mathematical and Physical Sciences **394**, 223–241 (1984). https://doi.org/10.1098/rspa.1984.0077

24. Kim, J., Yin, X., Tsao, K. C., Fang, S. & Yang, H. $Ca_2Mn_2O_5$ as oxygen-deficient perovskite electrocatalyst for oxygen evolution reaction. *J. Am. Chem. Soc.* **136**, 14646–14649 (2014). https://doi.org/10.1021/ja506254g
25. Nardi, F. R. & Zocca, A. Tunneling behavior of Ising and Potts models in the low-temperature regime. *Stochastic Processes and their Applications* **129**, 4556–4575 (2019). https://doi.org/10.1016/j.spa.2018.12.001
26. Bet, G., Gallo, A. & Nardi, F. R. Critical Configurations and Tube of Typical Trajectories for the Potts and Ising Models with Zero External Field. *J. Stat. Phys.* **184**, 30 (2021). https://doi.org/10.1007/s10955-021-02814-1
27. Suescun, L., Hadermann, J. & Dabrowski, B. HR-TEM study of oxygen vacancy ordered $Sr_{4+n}Mn_{4+n}O_{10+3n}$ compounds. *Acta Crystallographica Section A* **70**, C942 (2014). Published microsymposium abstract MS62.O04. https://journals.iucr.org/a/issues/2014/a1/00/a52242/a52242.pdf
28. Steinegger, J., Banerjee, D., Huffman, E. & Rammelmüller, L. Geometric fragmentation and anomalous thermalization in cubic dimer model. *Phys. Rev. D* **112**, 114512 (2025). https://doi.org/10.1103/4kzq-t1zs
29. Rosenblatt, J. & Seymour, P. D. The Structure of Homometric Sets. *SIAM. J. on Algebraic and Discrete Methods* **3**, 343–350 (1982). https://doi.org/10.1137/0603035

Funding

This research received no external funding.

Author contributions

Jiasheng Yang: conceptualization, methodology, software, validation, formal analysis, investigation, data curation, writing – original draft, writing – review and editing, visualization, and project administration.

Competing interests

The author declares no conflict of interest.

Ethics

Institutional review board approval and informed consent are not applicable to this theoretical and computational study, which reports no new human or animal research.

Supplementary Files

This is a list of supplementary files associated with this preprint. Click to download.

- 02SupplementaryInformation.pdf